

Cite this: *J. Mater. Chem. A*, 2017, 5, 12557

# Platinum–nickel nanowire catalysts with composition-tunable alloying and faceting for the oxygen reduction reaction†

Fangfang Chang,<sup>ab</sup> Gang Yu,<sup>\*a</sup> Shiyao Shan,<sup>b</sup> Zakiya Skeete,<sup>b</sup> Jinfang Wu,<sup>b</sup> Jin Luo,<sup>b</sup> Yang Ren,<sup>c</sup> Valeri Petkov<sup>id</sup><sup>\*d</sup> and Chuan-Jian Zhong<sup>id</sup><sup>\*b</sup>

The ability to tune the alloying properties and faceting characteristics of bimetallic nanocatalysts is essential for designing catalysts with enhanced activity and stability through optimizing strain and ligand effects, which is an important frontier for designing advanced materials as catalysts for fuel cell applications. This report describes composition-controlled alloying and faceting of platinum–nickel nanowires (PtNi NWs) for the electrocatalytic oxygen reduction reaction. The PtNi NWs are synthesized by a surfactant-free method and are shown to display bundled morphologies of nano-tetrahedra or nanowires, featuring an ultrathin and irregular helix morphology with composition-tunable facets. Using high-energy synchrotron X-ray diffraction coupled with atomic pair distribution function analysis, lattice expansion and shrinking are revealed, with the Pt : Ni ratio of  $\sim 3 : 2$  exhibiting a clear expansion, which coincides with the maximum electrocatalytic activity for the ORR. In comparison with PtNi nanoparticles (NPs), the PtNi NWs display remarkably higher electrocatalytic activity and stability as a result of the composition-dependent atomic-scale alloying and faceting, demonstrating a new pathway to the design of alloy nanocatalysts with enhanced activity and durability for fuel cells.

Received 14th April 2017  
Accepted 16th May 2017

DOI: 10.1039/c7ta03266h

rsc.li/materials-a

## 1. Introduction

Proton exchange membrane fuel cells (PEMFCs) have become an increasingly attractive power source because of their high efficiency and zero pollution.<sup>1</sup> The ultimate commercialization, however, must address a key challenge for the sluggish reaction kinetics at the cathode, *i.e.*, the oxygen reduction reaction (ORR), which requires not only highly active but also stable and low-cost catalysts.<sup>2</sup> Although Pt catalysts are considered to be active cathode electrocatalysts for the ORR, their high cost and

limited global supply makes it imperative to moderate the usage of Pt in the application process.<sup>3</sup> One important approach is to alloy Pt with low-cost transition metals in nanoscale materials. In comparison with nanoparticles, nanowires/nanofibers have many intriguing attributes in terms of surface properties. The formation of the network structure with open-access porosity for nanowires/nanofibers leads to an increased accessibility to the surface or an increased effective surface area. For example, polypyrrole nanowires show a higher specific surface area than nanoparticles by a factor of 15, as indicated by a Brunauer–Emmett–Teller (BET) study.<sup>4</sup> Nanofiber catalysts with porous and diameter-controlled structures have been shown to exhibit high specific surface area and specific activity compared with nanoparticle catalysts.<sup>5,6</sup> Recently, PtNi alloy nanowires, prepared by converting Pt/NiO core/shell nanowires through a thermal annealing process followed by transformation into jagged Pt nanowires *via* electrochemical dealloying, have been shown to exhibit a greatly enhanced mass activity for the ORR.<sup>7</sup> One-dimensional (1D) Pt-based nanostructures have been shown to display higher catalytic activities towards the ORR than zero-dimensional (0D) Pt nanoparticles.<sup>8</sup> It is suggested that there is a stronger interaction of NWs with carbon supports and less vulnerable dissolution of metals than conventional nanoparticle counterparts which have a propensity to Ostwald ripening and aggregation in strongly acidic conditions.<sup>9</sup> The activity enhancements are generally attributed to several factors,<sup>10</sup> including a 1D structure that favors reaction mass

<sup>a</sup>College of Chemistry and Chemical Engineering, Hunan University, Changsha 410082, China. E-mail: yuganghnu@163.com

<sup>b</sup>Department of Chemistry, State University of New York at Binghamton, Binghamton, New York 13902, USA. E-mail: cjzhong@binghamton.edu

<sup>c</sup>X-ray Science Division, Advanced Photon Source, Argonne National Laboratory, Argonne, Illinois 60439, USA

<sup>d</sup>Department of Physics, Central Michigan University, Mt. Pleasant, Michigan 48859, USA. E-mail: petko1vg@cmich.edu

† Electronic supplementary information (ESI) available: The information includes the following contents: Fig. S1, TEM images and EDX spectrum of PtNi NWs; Fig. S2, TEM images of NWs and NPs; Table S1, plot of percentages of relative facet domain sizes,  $S(200)$  vs.  $S(111)+S(200)$ ; Scheme S1, models of NWs and NPs; Fig. S3, XRD patterns of NWs and NPs; Fig. S4, XRD patterns of NWs; Table S2, current extraction in the kinetic region of PtNi NWs/C catalysts; Table S3, comparison of compositions, and ORR activities of different PtNi alloy catalysts; Fig. S5, durability of commercial Pt/C; Fig. S6, durability test of the Pt<sub>59</sub>Ni<sub>41</sub> NWs/C catalyst for the ORR; electrocatalytic activity measurement. See DOI: 10.1039/c7ta03266h

transport with a reduced activation energy, an extended surface structure that weakens interactions with oxygenated species (*i.e.*, OH<sub>ad</sub>) for improving reaction kinetics,<sup>11</sup> and increased surface area to volume ratio in comparison with nanoparticle counterparts.<sup>4</sup> There are also studies showing porous hollow PtNi/C nanostructures for increasing mass activity and specific activity up to 6–9 times as compared with standard Pt/C catalysts.<sup>12</sup> The octahedral alloy PtNiNPs synthesized by the solvothermal method without any surfactant with a particle size of 9 nm showed a 10-time increase in specific activity and mass activity compared with commercial Pt/C catalysts.<sup>13</sup>

In our recent work, we have demonstrated the synthesis of PtAu NWs with a Boerdijk–Coxeter helix type of structure featuring (111) facet-dominant surfaces for increasing the electrocatalytic activity and stability for the ORR.<sup>14</sup> However, for NWs of Pt alloyed with non-noble base metals, this type of structure-tuned catalytic synergy has not been reported. Herein, we report the first example of PtNi NWs with composition-tunable (111)/(200) facets and the enhanced electrocatalytic synergy for the oxygen reduction reaction. Important insights into the structure–activity correlation are gained with the help of high-resolution transmission electron microscopy to determine the crystalline facets and synchrotron high-energy X-ray diffraction (HE-XRD) coupled to atomic pair distribution function (PDF) analysis to probe the atomic-scale alloying properties.

## 2. Experimental section

### 2.1 Chemicals

Platinum(II) acetylacetonate (Pt(acac)<sub>2</sub>, 97%) was obtained from Alfa Aesar. Nickel(II) acetylacetonate (Ni(acac)<sub>2</sub>, >95%), potassium hydroxide (KOH, 85+%), ethylene glycol anhydrous (EG, 99.8%), *N,N*-dimethylformamide (DMF, 99.8%) and Nafion (5 wt%) were obtained from Aldrich. Ethanol (200 proof, ACS grade), hexane (99.9%) and potassium chloride were obtained from Fisher. Carbon black (Vulcan XC-72) was purchased from Cabot. A Millipore Milli-Q water system was used to purify deionized water (DI water). The E-tek Pt/C catalyst (20 wt% metal loading) was purchased from Strem Chemicals. All gases such as oxygen, nitrogen and hydrogen were obtained from Airgas.

### 2.2 Synthesis and preparation of catalysts

Pt<sub>*n*</sub>Ni<sub>100–*n*</sub> NWs were synthesized by a modified hydrothermal method.<sup>15,16</sup> Briefly, KOH (6.0 g) was dissolved in a solution containing DMF (60 mL) and EG (36 mL). After KOH was completely dissolved, Pt(acac)<sub>2</sub> (47.5 mg) and Ni(acac)<sub>2</sub> (51.0 mg) were added to the solution mixture. The ultrathin Pt<sub>*n*</sub>-Ni<sub>100–*n*</sub> NWs of different compositions were controlled by the feed molar ratio. After magnetic stirring overnight, the resultant homogeneous and transparent solution was transferred into a Teflon-lined autoclave (size: 100 mL) and then maintained at 180°C for 8 h. After that, the autoclave was cooled to room temperature. The resulting Pt<sub>*n*</sub>Ni<sub>100–*n*</sub> NWs were then collected

by centrifugation. After washing with ethanol several times, the Pt<sub>*n*</sub>Ni<sub>100–*n*</sub> NWs were redispersed in DI water for future use.

The preparation involved assembly of the nanowires on a support, followed by thermochemical processing for activation of the catalysts. To prepare NWs on XC-72 carbon, a certain amount of carbon was dispersed in aqueous solution by ultrasonication and then the resulting Pt<sub>*n*</sub>Ni<sub>100–*n*</sub> nanowires were added to the well-dispersed carbon suspension under vigorous stirring for 30 min. To remove the capping agent (amines) and to deposit Pt<sub>*n*</sub>Ni<sub>100–*n*</sub> nanowires on carbon, ethanol (150 mL) was added to the above solution to form Pt<sub>*n*</sub>Ni<sub>100–*n*</sub> NWs/C catalysts. The Pt<sub>*n*</sub>Ni<sub>100–*n*</sub> NWs/C powder was collected by centrifugation and dried in an oven at 70°C overnight. The thermogravimetric analysis (TGA) performed on a PerkinElmer Pyris 1-TGA, which was used to determine the mass loading of catalysts. The mass loadings of PtNi NW catalysts described here were within 15–20 wt% (*e.g.*, 20% for Pt<sub>43</sub>Ni<sub>57</sub> NWs/C, 17% for Pt<sub>78</sub>Ni<sub>22</sub> NWs/C, 16% for Pt<sub>59</sub>Ni<sub>41</sub> NWs/C, 15% for Pt<sub>92</sub>Ni<sub>8</sub> NWs/C, Pt<sub>24</sub>Ni<sub>76</sub>NPs/C and Pt NWs/C).

Pt<sub>59</sub>Ni<sub>41</sub> nanoparticles were prepared similarly by increasing platinum and nickel feed concentrations and decreasing the reaction time for comparison. Briefly, to prepare Pt<sub>59</sub>Ni<sub>41</sub>NPs, KOH (1.0 g) was dissolved in a solution containing DMF (6 mL) and EG (4 mL). Pt(acac)<sub>2</sub> (48.6 mg) and Ni(acac)<sub>2</sub> (79.5 mg) were added to the above solution mixture after the KOH was completely dissolved. After magnetic stirring overnight, the resultant homogeneous and transparent solution was transferred into a Teflon lined autoclave (size: 20 mL). The autoclave was heated and maintained at 180°C for 1 h and then cooled down to room temperature. The resulting PtNiNPs (Pt<sub>59</sub>Ni<sub>41</sub>) were collected by washing and centrifugation. The Pt<sub>59</sub>Ni<sub>41</sub>NPs were supported on carbon and dried in an oven overnight and the weight loading of Pt<sub>59</sub>Ni<sub>41</sub>NPs/C was determined to be 19%.

### 2.3 Characterization of catalysts

**Inductively coupled plasma-optical emission spectroscopy (ICP-OES).**<sup>17</sup> The chemical compositions of the PtNi NWs were analyzed by ICP-OES. The standards were analyzed as a check. If the standards did not fall within ±5%, instrument recalibration was performed.

**Transmission electron microscopy (TEM).** TEM was used to determine the morphology of PtNi NWs. The analysis was done with an FEITecni G2 F20 microscope operating at 200 kV by drop casting the dispersions of NWs on carbon-coated copper grids. The uniformity of the PtNi NWs/C was analyzed by high-angle annular dark-field scanning TEM (HAADF-STEM) imaging and EDX spectroscopy.

**X-ray photoelectron spectroscopy (XPS).** The samples were collected from initial and 5000 electrochemical cycles and analyzed by XPS, which was performed on an Escalab 250Xi instrument. The international standard (C 1s) was used to calibrate the peak position.

**High energy X-ray diffraction (HE-XRD) experiments and atomic pair distribution function (PDF) derivation.** The synchrotron HE-XRD (The Advanced Photon Source (Sector-11) at Argonne National Laboratory) was used to characterize the

PtNi NWs/C catalysts. Data were taken using X-rays with a wavelength,  $\lambda$ , of 0.1080 Å (X-ray energy ~115 keV). The carbon supported nanowire or nanoparticle catalyst samples were sealed inside a thin-walled glass capillary (1.5 mm in diameter). The measurement was performed at room temperature. Experimental HE-XRD patterns were reduced to structure factors,  $S(q)$ , before Fourier transformation to atomic pair distribution functions (PDFs)  $G(r)$ . Note that  $G(r)$  oscillates around zero, showing positive peaks at real space distances ( $r$ ).

## 2.4 Electrochemical measurements

The glassy carbon (GC) disks were polished with 0.005  $\mu\text{m}$   $\text{Al}_2\text{O}_3$  powders. The catalyst inks were prepared by suspending PtNi NWs on carbon (5 mg) into a 5 mL mixture of water, 2-propanol and Nafion (4.5 : 0.25 : 0.25, v/v/v) which was ultrasonicated for at least 40 min to form a homogeneous ink. Then 10  $\mu\text{L}$  ink was transferred to the surface of the GC disk.<sup>18</sup> The electrochemical CH instruments (CHI600a) were used to measure Cyclic Voltammetry (CV) and Rotating Disk Electrode (RDE) curves with a three-electrode electrochemical cell. The electrolyte solution (0.1 M  $\text{HClO}_4$ ) was de-aerated with  $\text{N}_2$  (99.99%) before CV measurements, and then  $\text{O}_2$ -saturated for RDE measurements. The reference electrode was a reversible hydrogen electrode (RHE) and the experiments were performed at room temperature.

## 2.5 Computational modeling

*Ab initio* and DFT calculations were performed using density functional theory with DMol3 program coming as a part of Materials Studio software.<sup>19</sup> The computations used generalized gradient approximation with the exchange correlation function.<sup>20</sup> It involved the localized double numerical basis sets and polarization functions for the valence orbitals, and effective core potential to account for the core electrons of metallic species. Full geometry optimizations were performed for all model atomic configurations tested here, so that all atoms were fully relaxed. The unsupported small  $\text{Pt}_n\text{Ni}_{12-n}$  model configurations were included. The adsorbed energies of atomic oxygen on the  $\text{Pt}_n\text{Ni}_{12-n}$  model were used as a measure of the adsorbed strength of O adsorption. It was calculated as  $E_{\text{ads}} = -(E_{\text{O-metal}} - E_{\text{metal}} - E_{\text{O}})$ , where  $E_{\text{O-metal}}$ ,  $E_{\text{metal}}$  and  $E_{\text{O}}$  are the total energies of the O-metal, the metal atomic configuration, and the isolated O molecule, respectively.<sup>21</sup>

# 3. Results and discussion

## 3.1 Composition and morphology of PtNi NWs

The synthesis strategy is based on a single-phase and surfactant-free synthesis route, in which  $\text{Ni}(\text{acac})_2$  and  $\text{Pt}(\text{acac})_2$  with controlled ratios are used in combination with controlled amounts of potassium hydroxide, ethylene glycol, and *N,N*-dimethylformamide to produce PtNi NWs of different compositions. A typical set of TEM images are shown in Fig. 1 for the as-synthesized PtNi NWs with different compositions (see also the data obtained from ICP-OES and EDX spectroscopy, Fig. S1, ESI†). The nanowires are very thin, featuring a diameter of 3.3  $\pm$

0.5 nm and show a tendency of forming a network-like structure consisting of bundles of closely-spaced or interconnected nanowires. This feature could be due to the propensity of forming active defects along the nanowires, which leads to coalescence upon contacting different nanowires, forming network structures. It is interesting to note that the structural defects,<sup>22,23</sup> such as grain boundaries and vacancies, could contribute to the catalytic enhancement. Another possibility is that there is a strong cohesive interaction along the nanowires driven by the minimization of the total surface free energy, which is aided by hydrophobic interactions of DMFs being adsorbed on the NWs' surface during the synthesis of PtNi NWs. This type of morphology was not observed for PtNiNPs.

The individual NWs in a bundle are ultrathin and run in parallel to each other (Fig. 2 upper). Note that in the case of  $\text{Pt}_{22}\text{Ni}_{78}$ , it cannot form nanowires, but form particulate nanostructures with only (111) facets, just like several tetrahedra packing.<sup>24</sup> The compositions and distribution of the as-synthesized PtNi NWs were analyzed using HAADF-STEM imaging and EDX spectroscopy. Fig. 2 lower panel shows that the distributions of Pt and Ni elements are homogeneous in the NW bundles. Similar features characteristic of the (111) and (200) facets along the nanowires have also been observed for PtNi NWs of the other compositions.

Fig. 3 shows a detailed comparison of (111) and (200) facets identified for PtNi NWs of different compositions. With increasing Pt%, (200) facets increase, or the relative (111) to (200) ratio decreases (Table S1, ESI†), indicating the important role of Pt in the faceting of the nanowires.

Importantly, the relative ratio of (200) facets vs. all facets ((200) and (111)) being identified is found to be dependent on the composition (see Table S1, ESI†). The relative ratio was estimated from the ratios of the areas of (111) and (200) visualized in HR-TEM images, including those in Fig. 3 and in ESI.† As Pt% increases from 0 to ~45%, the ratio is basically zero. As Pt% increases from ~50% to higher, the ratio showed a sharp increase in the range of 10 to 25%. As Pt% increases, the emergence of 200-facets reduces the coordination number and so increases the bonding distance for near-surface Pt atoms. In other words, the Pt-Pt bond length is effectively increased, which is consistent with the XRD data. There is, thus, a change in the electronic structure of surface Pt atoms, which is responsible for a change in the d-band center in a way towards enhancing the ORR activity. In contrast, both PtNiNPs and Pt NWs feature only (111) facets (see Fig. S2, ESI†).

The average lattice fringes of (111) and (200) atomic planes were found to fall in between pure Ni and pure Pt, indicative of an alloy-type structure. Interestingly, the PtNi NWs seem to feature an irregular Boerdijk-Coxeter type helix, resembling somewhat to those found in  $\gamma$ -Cu, Au, AuAg, AuCu and AuPt nanowires.<sup>14,24-27</sup> The PtAu nanowires with controlled compositions exhibited a Boerdijk-Coxeter helix type of structure featuring (111) facet-dominant surfaces,<sup>14</sup> whereas the PtNi NWs showed an irregular Boerdijk-Coxeter type helix. An aggregative growth mechanism may be operative for the composition-dependent formation of the bundled NWs and the

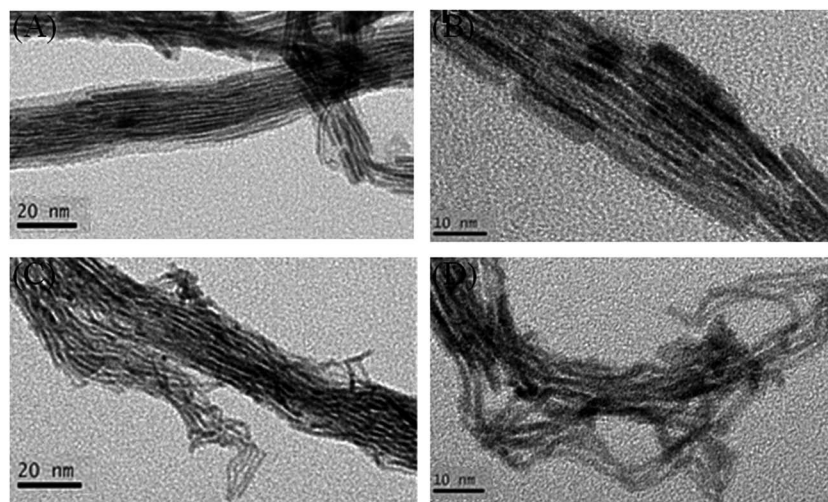


Fig. 1 TEM images of the nanowire samples  $\text{Pt}_{42}\text{Ni}_{58}$  (A and B) and  $\text{Pt}_{88}\text{Ni}_{12}$  (C and D). The average diameter of individual nanowires in the bundles is  $3.3 \pm 0.5$  nm (A) and  $3.3 \pm 0.5$  nm (B).

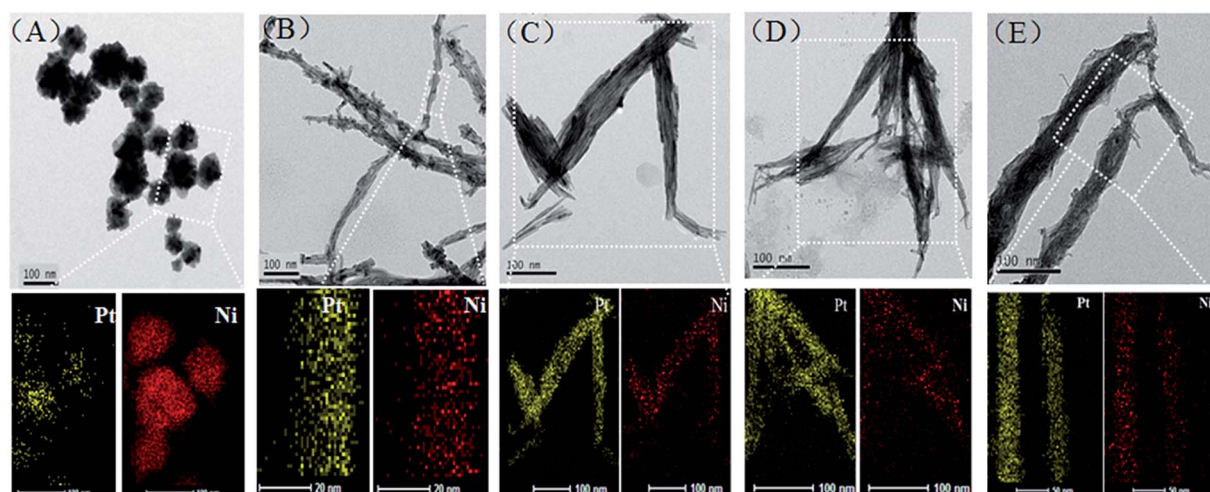


Fig. 2 TEM images (top panel) and elemental maps of Pt and Ni (bottom panel) for  $\text{Pt}_n\text{Ni}_{100-n}$  ( $n = 22$  (A), 42 (B), 57 (C), 75 (D) and 88 (E)) NWs (Pt species are in yellow, and Ni species are in red).

cluster-like features (see Scheme S1, ESI<sup>†</sup>). A similar model was reported for the cluster-like features, but in different systems.<sup>24</sup>

In addition to in-house XRD patterns for NWs and NPs, which showed some differences for (111) and (200) between NWs and NPs (Fig. S3 and S4, ESI<sup>†</sup>). Note that the in-house XRD pattern features are broad and sometimes complicated to index due to the small diameters of nanowires and their bundling. In this regard, HE-XRD/PDF provides valuable information for the structural analysis. The structures of PtNi NWs were examined by HE-XRD to determine the dependence of NW structures on the compositions. Fig. 4A shows a representative set of atomic PDFs, which were extracted from the HE-XRD patterns of  $\text{Pt}_n\text{Ni}_{100-n}$  NWs.

The lattice parameters extracted from fcc-type fits to the experimental PDF data are summarized in Fig. 4B. Lattice parameters of bulk Pt and Ni are also included for comparison. While the data are in general very close to the linear

relationship, characteristic of alloying according to Vegard's law based on the lattice parameters of Ni and Pt, there are subtle differences in terms of small deviations from the linear relation simply based on Ni and Pt lattice parameters. In particular, such deviations appear to depend on the morphology of the nanomaterials. There is a lattice expansion when Pt% is greater than  $\sim 40\%$  and less than  $\sim 90\%$  but a small lattice shrinking when Pt% is less than  $\sim 40\%$  and greater than  $\sim 90\%$ . This result is also confirmed by in-house XRD data (see Fig. S4B, ESI<sup>†</sup>). While the lattice expansion and shrinking depends on the composition, the NWs derived from the Pt : Ni ratio of  $\sim 3 : 2$  exhibit a clear expansion.

The NW compositions, sizes and loading data are summarized in Table 1 for PtNi/C catalysts, with the loading being controlled in the range of 15–20%. Note that the nanoparticles and nanowires are homogeneous in composition within the

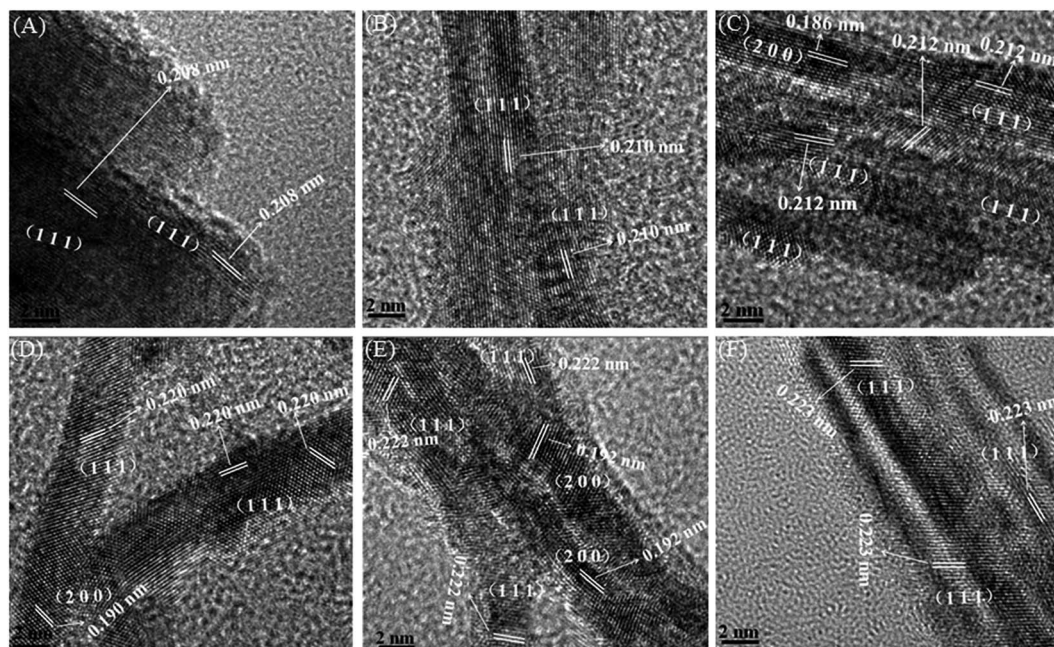


Fig. 3 HR-TEM images of  $\text{Pt}_n\text{Ni}_{100-n}$  NWs ( $n = 22$  (A), 42 (B), 57 (C), 75 (D), 88 (E) and 100 (F)), with lattice fringes and corresponding facets being indicated.

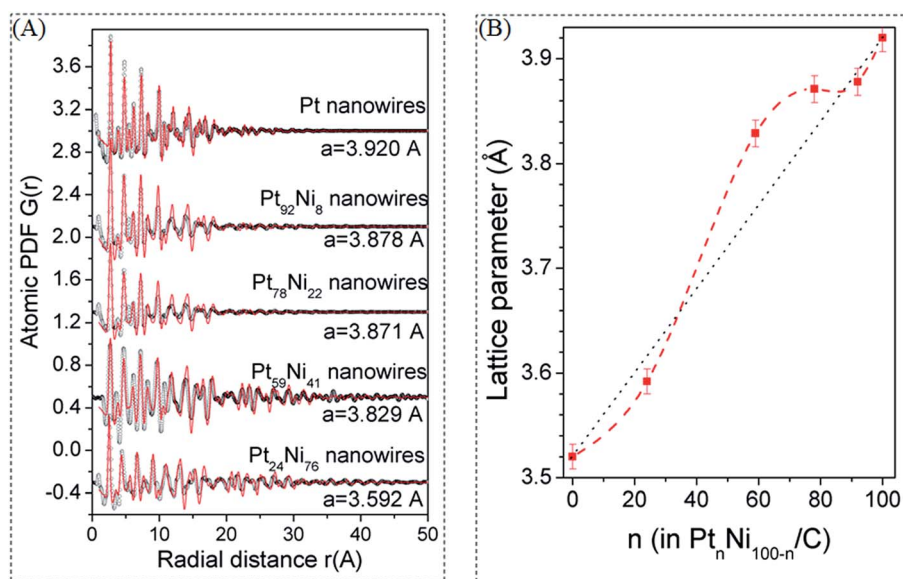


Fig. 4 (A) Experimental (symbols) and fcc-model fit (red line) atomic PDFs for pure Pt and PtNi NWs. (B) Plots of PDF-fit derived fcc lattice parameters:  $\text{Pt}_n\text{Ni}_{100-n}$  NWs (red squares). The dotted red line provides a general guide to the trend of the data points for NWs. The dotted black line tracks the prediction of Vegard's law based on the lattice parameters of Ni and Pt.

samples, as supported by the XRD data showing no indication of phase segregation.

### 3.2 Electrocatalytic properties for the oxygen reduction reaction

**Catalyst activities.** The PtNi NWs were used as catalysts and directly tested to determine their electrocatalytic ORR properties without any surface treatment in terms of electrochemical

active area (ECA), mass activity (MA), and specific activity (SA), which were determined from the measurement of CV and RDE curves, as described in previous reports.<sup>28–31</sup> CV curves were measured after 30 potential cycles between 0.05 and 1.2 V (vs. the RHE) at 50  $\text{mVs}^{-1}$  in 0.1 M  $\text{HClO}_4$  saturated with  $\text{N}_2$  at room temperature. The voltammetric peak characteristics of the alloy NWs in the region of hydrogen adsorption/desorption (Fig. 5A) show subtle dependence on the composition. Note that the

**Table 1** Summary of particle sizes and lattice constants of PtNi NWs/C catalysts

Catalysts	NWs size (nm)	Metal loading (% wt)	Lattice parameter (nm)	Scherrer size (nm)
Pt <sub>24</sub> Ni <sub>76</sub> /C	20.0±2.0	15%	0.3703	20.5±2.1
Pt <sub>43</sub> Ni <sub>57</sub> /C	3.3±0.5	20%	0.3829	3.6±0.7
Pt <sub>59</sub> Ni <sub>41</sub> /C	2.0±0.5	16%	0.3859	2.2±0.4
Pt <sub>78</sub> Ni <sub>22</sub> /C	3.0±0.6	17%	0.3879	3.1±0.7
Pt <sub>92</sub> Ni <sub>8</sub> /C	3.0±0.5	15%	0.3896	3.3±0.4
Pt/C	2.0±0.2	15%	0.3920	2.3±0.5

general characteristic of the hydrogen adsorption waves for the NWs is similar to those reported in the literature.<sup>32</sup> The measurement was typically repeated several times to ensure reproducibility. The peaks feature characteristics of the (110) facet at 0.12 V and contributions associated with (100)/(111) terraces at 0.24 V.<sup>33</sup> For PtNi and Pt NWs, the peak associated with the (111) or (100)/(111)<sup>34</sup> facet appears to be dominant, whereas the peak attributed to (110) diminishes. The dominance of the (111)-associated peak appears to be most significant for Pt<sub>59</sub>Ni<sub>41</sub> NWs. In terms of peak currents, Pt<sub>59</sub>Ni<sub>41</sub> NWs exhibit the largest peak current, whereas Pt<sub>24</sub>Ni<sub>76</sub> NWs show the smallest one. ECA values of the PtNi NWs (Fig. 5B), which were determined from the charges integrated under the hydrogen adsorption waves,<sup>35</sup> also exhibit clear dependence on the bimetallic composition and particle size, revealing a maximum value (54 m<sup>2</sup> g<sub>Pt</sub><sup>-1</sup>) for n~59%Pt, which is greater than that of Pt NWs/C (50 m<sup>2</sup> g<sub>Pt</sub><sup>-1</sup>).

A clear difference of the current in the kinetic region of the RDE curves is revealed for the NW catalysts of different bimetallic compositions, as shown in Fig. 6A. The extraction of the current in the kinetic region for assessment of the mass and specific activities is well established, as documented in many of our previous publications.<sup>36,37</sup> The kinetic currents (Table S2, ESI†) are much smaller than the currents in the diffusion region, ensuring the kinetic assessment. Note that there were some variations of the diffusion currents in the RDE curves, which, we believe, is partly caused by the lack of uniformity of the catalyst layer cast on the electrode surface. Considering the

differences in Pt loading (*i.e.*, 7.0, 15.0, 13.0, 15.0, 14.0 and 15.0% for Pt<sub>24</sub>Ni<sub>76</sub>NPs/C, Pt<sub>43</sub>Ni<sub>57</sub> NWs/C, Pt<sub>59</sub>Ni<sub>41</sub> NWs/C, Pt<sub>78</sub>Ni<sub>22</sub> NWs/C, Pt<sub>92</sub>Ni<sub>8</sub> NWs/C and Pt NWs/C, respectively), changes of the kinetic currents at 0.900 V (*vs.* the RHE, Fig. 6A) for these catalysts were normalized against the Pt loading in terms of MA and SA. The mass activity (Fig. 6B) strongly depends on the bimetallic compositions and particle size, revealing a maximum for Pt<sub>59</sub>Ni<sub>41</sub> NWs. The SA trend of the relative facets from (111) appears to show a similar trend. A maximum activity is revealed at a Pt : Ni ratio of ~3 : 2. The mass activity increases with Pt, reaching a maximum for Pt<sub>59</sub>Ni<sub>41</sub> NWs, which appears to follow the (100) dominance. It is reported that the ORR catalytic activity on Pt<sub>3</sub>Ni nanooctahedra with the (111) facet is almost 5 times higher than that of nanocubes with (100) facets.<sup>38</sup> To understand how this characteristic operates with the stability of PtNi NWs in this work, we mainly focused on Pt<sub>59</sub>Ni<sub>41</sub> NWs/C for a detailed characterization.

The electrocatalytic data of PtNi NWs/C catalysts are summarized in Table 2. It is clear that the activity is dependent not only on the bimetallic composition but also on the particle size. The catalyst was found to show a higher mass activity with a higher Pt% composition. The mass activity and ECA were found to increase with the decrease in the nanowire size, reaching a maximum at 2.1 nm.

There are several studies of PtNi nanocatalysts with different shapes and compositions with very high catalytic activities for the ORR. For example, the Pt-rich PtNi octahedral NPs synthesized by a solvothermal method showed relatively high ORR activities.<sup>39</sup> Pt<sub>x</sub>Ni<sub>1-x</sub> alloy NPs synthesized using organic solvents revealed that the extent of Ni depletion and the formation of a Pt-skeleton structure in the near-surface region determine the catalytic properties, which depended on the initial composition.<sup>40</sup> Pt<sub>3</sub>Ni<sub>1</sub>NPs synthesized on carboxylic acid-functional multiwalled carbon nanotubes showed 2–3 times higher activity than Pt/C.<sup>41</sup> In comparison with the ORR activities of other PtNi nanowire or nanoparticle catalysts reported in the literature (Table S3, ESI†),<sup>39–47</sup> the data for our PtNi nanowire catalysts show a competitive performance under the condition of no post-synthesis treatment of the catalysts.

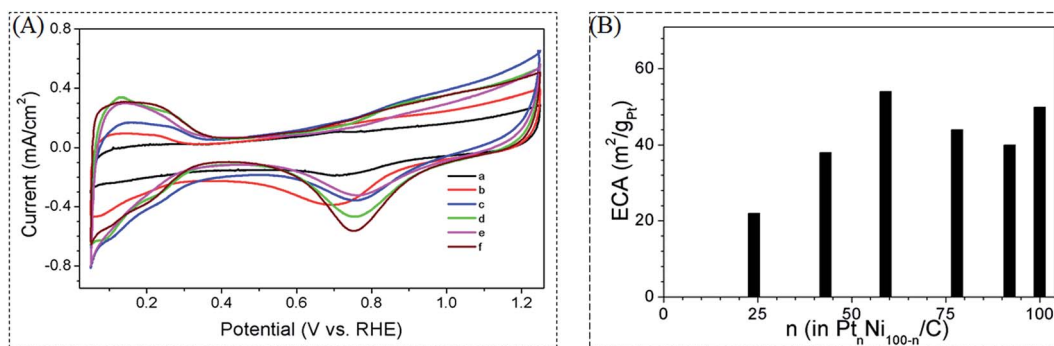


**Fig. 5** (A) CV curves of Pt<sub>n</sub>Ni<sub>100-n</sub> NWs of different bimetallic compositions: Pt<sub>24</sub>Ni<sub>76</sub>NPs/C (a, black), Pt<sub>43</sub>Ni<sub>57</sub> NWs/C (b, red), Pt<sub>59</sub>Ni<sub>41</sub> NWs/C (c, blue), Pt<sub>78</sub>Ni<sub>22</sub> NWs/C (d, green), Pt<sub>92</sub>Ni<sub>8</sub> NWs/C (e, magenta) and Pt NWs/C (f, wine). Electrode: glassy carbon (0.196 cm<sup>2</sup>) inked with 10 μg catalysts; electrolyte: 0.1 M HClO<sub>4</sub> saturated with N<sub>2</sub>; scan rate: 50 mVs<sup>-1</sup>; (B) ECA values *vs.* Pt%.

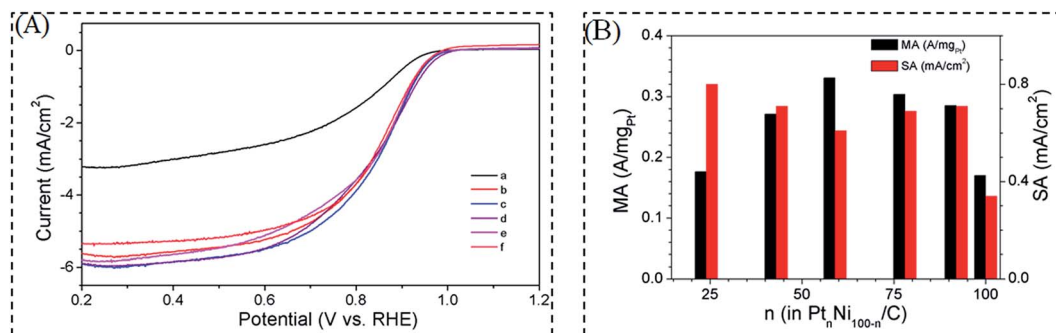


Fig. 6 (A) RDE curves of  $\text{Pt}_n\text{Ni}_{100-n}$  NWs of different bimetallic compositions:  $\text{Pt}_{24}\text{Ni}_{76}$  NPs/C (a, black),  $\text{Pt}_{43}\text{Ni}_{57}$  NWs/C (b, red),  $\text{Pt}_{59}\text{Ni}_{41}$  NWs/C (c, blue),  $\text{Pt}_{78}\text{Ni}_{22}$  NWs/C (d, purple),  $\text{Pt}_{92}\text{Ni}_8$  NWs/C (e, magenta) and Pt NWs/C (f, pink). Electrode: glassy carbon ( $0.196\text{ cm}^2$ ) inked with  $10\text{ }\mu\text{g}$  catalysts; electrolyte:  $0.1\text{ M HClO}_4$  saturated with  $\text{O}_2$ ; scan rate:  $10\text{ mVs}^{-1}$ ; and rotation speed:  $1600\text{ rpm}$ ; (B) mass activity (MA) and specific activity (SA) data at  $0.900\text{ V}$  (vs. the RHE).

Table 2 Summary of physical and electrocatalytic data for PtNi NWs/C catalysts<sup>a</sup>

Catalysts	NWs size on carbon (nm)	Metal loading (% wt)	Lattice parameter (nm)	ECA ( $\text{m}^2\text{g}_{\text{Pt}}^{-1}$ )	MA ( $\text{A}\text{mg}_{\text{Pt}}^{-1}$ )	SA ( $\text{mA}\text{cm}^{-2}$ )
$\text{Pt}_{24}\text{Ni}_{76}/\text{C}$	$20.1\pm 2.1$	15%	0.3703	22	0.176	0.80
$\text{Pt}_{43}\text{Ni}_{57}/\text{C}$	$3.4\pm 0.5$	20%	0.3829	38	0.271	0.71
$\text{Pt}_{59}\text{Ni}_{41}/\text{C}$	$2.1\pm 0.3$	16%	0.3859	54	0.330	0.61
$\text{Pt}_{78}\text{Ni}_{22}/\text{C}$	$3.2\pm 0.3$	17%	0.3879	44	0.303	0.69
$\text{Pt}_{92}\text{Ni}_8/\text{C}$	$3.4\pm 0.4$	15%	0.3896	40	0.285	0.71
Pt/C	$2.3\pm 0.6$	15%	0.3920	50	0.170	0.34

<sup>a</sup> Note: catalyst loading:  $10\text{ }\mu\text{g}$ . Electrode area:  $0.196\text{ cm}^2$ . Electrolyte:  $0.1\text{ M HClO}_4$ . Scan rate:  $10\text{ mVs}^{-1}$ , rotation speed:  $1600\text{ rpm}$ . MA and SA potential:  $0.900\text{ V}$  (vs. the RHE).

**Catalyst durability.** The stability or durability of NWs is a critical requirement of catalysts for fuel cell applications. This parameter was assessed by performing accelerated durability tests of  $\text{Pt}_{59}\text{Ni}_{41}$  NWs/C catalysts in  $0.1\text{ M HClO}_4$  solution saturated with nitrogen gas by continuous potential cycling between  $0.6$  and  $1.1\text{ V}$  at room temperature. After  $5000$  cycles for  $\text{Pt}_{59}\text{Ni}_{41}$  NWs/C, the ECA shows a small increase from  $52$  to  $61\text{ m}^2\text{ g}^{-1}$  (Fig. 7A). A comparison of the RDE curves (Fig. 7B) reveals a change of the half-wave potential ( $E_{1/2}$ ) after  $5000$  cycles by  $\sim 10\text{ mV}$ . The mass activity extracted from the kinetic current in the RDE data ( $0.31\text{ A mg}_{\text{Pt}}^{-1}$ ) is shown to decrease only by  $\sim 9\%$  in comparison with that before  $5000$  cycles ( $0.28\text{ A mg}_{\text{Pt}}^{-1}$ ) (Fig. 7C). The durability of commercial Pt/C was also tested for comparison with  $\text{Pt}_{59}\text{Ni}_{41}$  NWs/C catalysts, as shown in Fig. S5, ESI†. The ECA was found to decrease from  $88$  to  $50\text{ m}^2\text{ g}^{-1}$  after  $5000$  cycles (Fig. S5A, ESI†). The half-wave potential ( $E_{1/2}$ ) also showed a shift of about  $\sim 25\text{ mV}$  after  $5000$  cycles (Fig. S5B, ESI†). The mass activity extracted from the kinetic current in the RDE data ( $0.09\text{ A mg}_{\text{Pt}}^{-1}$ ) is shown to decrease by  $\sim 55\%$  in comparison with that before the  $5000$  cycles ( $0.05\text{ A mg}_{\text{Pt}}^{-1}$ ) (Fig. S5C, ESI†). This result clearly shows that the  $\text{Pt}_{59}\text{Ni}_{41}$  NWs/C is remarkably durable as a catalyst for the ORR. A similar result was also obtained for the durability test of the same catalyst in  $0.1\text{ M HClO}_4$  solution saturated with oxygen gas by repetitive potential cycling (see Fig. S6, ESI†).

For understanding how the Ni composition changes in the PtNi NW catalysts during the ORR, the electrochemical method was efficient for assessing Ni leaching in relation to electrochemical performance.<sup>36</sup> This assessment could also be obtained using a concentrated acid to remove Ni, which is another method to be tested in future work. To further assess the electrochemically induced surface structural and compositional changes in the NWs, samples of the NWs were analyzed by TEM, ICP-OES and XPS after a certain number of potential cycles. The morphology of  $\text{Pt}_{59}\text{Ni}_{41}$  NWs/C remained largely intact (Fig. 8A). The lattice fringes of the (111) facets ( $0.221\text{ nm}$ ) showed a small change as compared with those before potential cycling (Fig. 8B and C). This reflects a Pt-rich surface after potential cycles, which was confirmed by TEM-EDX and ICP-OES (see Fig. 8D), which is consistent with the small increase of ECA after the potential cycles.

The comparison of the binding energies and elemental compositions from the XPS analysis (Fig. 9) provided additional insight into the relative surface composition of the catalysts. Before potential cycling, Pt 4f peaks were detected at  $71.1$  and  $74.4\text{ eV}$  for Pt  $4f_{7/2}$  and Pt  $4f_{5/2}$  ( $\text{Pt}^0$ ), respectively. After potential cycling, the binding energies,  $71.2$  and  $74.5\text{ eV}$ , remain essentially unchanged (Fig. 9A). However, for Ni 2p peaks (Fig. 9B), there is a significant positive shift for the binding energy ( $0.7\text{ eV}$ ), which is detected after the potential cycling. Ni  $2p_{3/2}$  is shifted from  $852.7$  to  $853.4\text{ eV}$ . A significant change is also

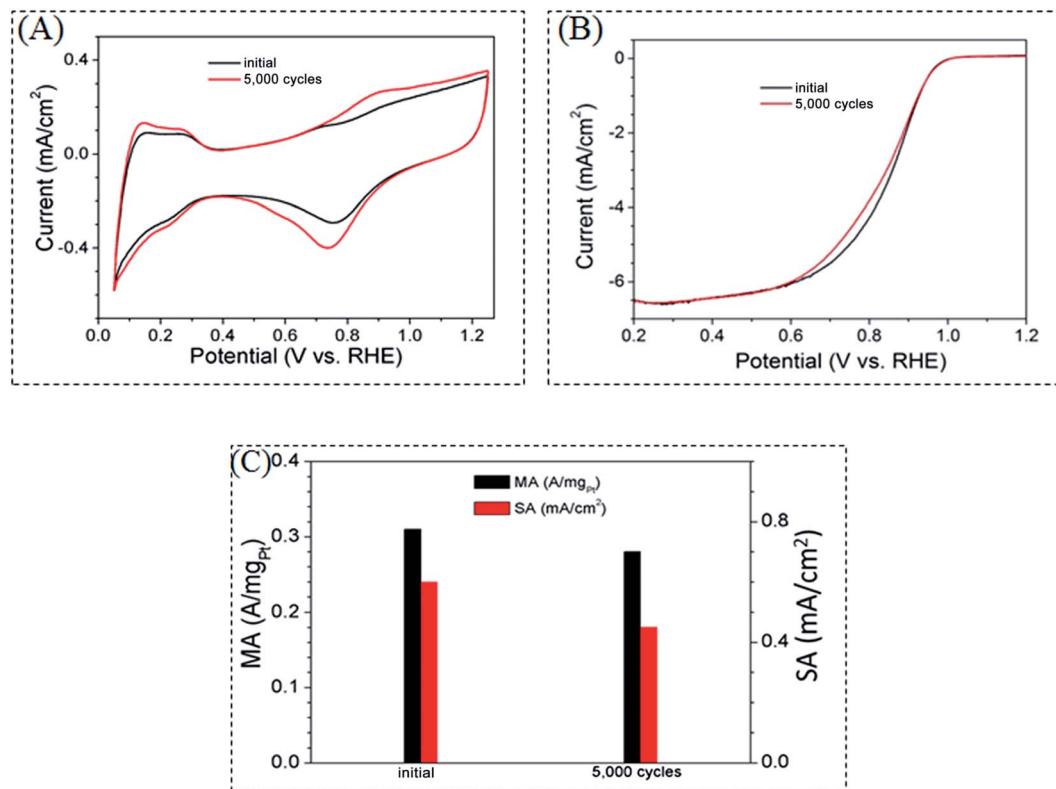


Fig. 7 (A) CV and (B) RDE curves of Pt<sub>59</sub>Ni<sub>41</sub> NWs/C before and after 5000 potential cycles (sweep rate, 50 mV s<sup>-1</sup>, potential cycle window: 0.6 and 1.1 V) in 0.1 M HClO<sub>4</sub> solution saturated with nitrogen and oxygen (scan rate: 10 mV s<sup>-1</sup> and rotation speed: 1600 rpm); (C) mass activity and specific activity data at 0.900 V (vs. the RHE) before and after 5000 cycles.

observed for the Pt/Ni atomic ratio from 1.6 : 1.3 before cycling to 1.2 : 0.2 after cycling. The value of 1.6 : 1.3 reflects closely the composition of Pt<sub>59</sub>Ni<sub>41</sub>, whereas the value of 1.2 : 0.2 is suggestive of loss of Ni from the alloy catalyst. To understand these results, a Pt-enriched outmost surface is considered for the PtNi NWs after potential cycling. The electronegativity of Pt is more than that of Ni, which may be responsible for a charge transfer from Ni to Pt. For the Pt-enriched surface, there is an increased number of Pt atoms, increasing the binding energy for Ni atoms. This assessment indeed agrees with the observed shift of the Ni 2p peak. For Pt, there is an insignificant peak shift reflecting an effective distribution of the charge by the increased number of Pt atoms, in agreement with the experimental data.

#### Comparison of catalytic properties between NWs and NPs.

The electrocatalytic activities of PtNi NWs are also compared with those of PtNi NPs for the ORR. PtNiNPs of similar compositions were synthesized by the same method for synthesizing the PtNi NWs with a different reaction condition (see the Experimental section). Fig. 10A shows a representative set of CV curves of Pt<sub>59</sub>Ni<sub>41</sub> NWs/C, Pt<sub>59</sub>Ni<sub>41</sub>NPs/C, Pt NWs/C and commercial Pt/C catalysts in N<sub>2</sub>-purged 0.1 M HClO<sub>4</sub> solution at room temperature. There are subtle differences in the voltammetric characteristics in the hydrogen adsorption/desorption region (0–0.4 V) and the platinum oxidation/reduction region (0.6–0.8 V). As shown in Fig. 10A, the Pt<sub>59</sub>Ni<sub>41</sub> NWs/C

catalyst exhibits a larger hydrogen adsorption peak than the NP counterparts, indicative of a larger ECA value for the NWs (see Fig. 10B). The electrocatalytic ORR activities are compared by comparing the RDE curves in the saturated-oxygen 0.1 M HClO<sub>4</sub> electrolyte for Pt<sub>59</sub>Ni<sub>41</sub> NWs/C, Pt<sub>59</sub>Ni<sub>41</sub>NPs/C, Pt NWs/C and commercial Pt/C catalysts (Fig. 10C). There is a clear difference in the kinetic region of the ORR. The differences are assessed by comparing the mass activity and specific activity. As shown in Fig. 10D, the Pt<sub>59</sub>Ni<sub>41</sub> NWs/C exhibits a mass activity of 0.33 A mg<sub>Pt</sub><sup>-1</sup>, which is increased by a factor of 2.85 times compared with that of the Pt<sub>59</sub>Ni<sub>41</sub>NPs/C (0.13 A mg<sub>Pt</sub><sup>-1</sup>). The MA of Pt<sub>59</sub>Ni<sub>41</sub> NWs is increased by a factor of 1.9 times in comparison with that of Pt NWs, and ~3.7 times in comparison with that of commercial Pt (0.09 A mg<sub>Pt</sub><sup>-1</sup>) (Fig. 10D). This can be understood by considering the greatly increased surface area-to-volume ratio for the nanowires in comparison with nanoparticles. As evidenced by the experimental data, the ECA of Pt<sub>59</sub>Ni<sub>41</sub> NWs is 2.7 times larger than that of Pt<sub>59</sub>Ni<sub>41</sub>NPs. Because of the great increase in the ECA of Pt<sub>59</sub>Ni<sub>41</sub> NWs, which is much more significant than the mass activity, the specific activity of Pt<sub>59</sub>Ni<sub>41</sub> NWs is thus smaller than that of the Pt<sub>59</sub>Ni<sub>41</sub>NPs. The results demonstrate that the NWs, as electrocatalysts for the ORR, are much superior to the NP counterparts in terms of mass activity.

**Catalytic synergy.** For the observed enhancement of the electrocatalytic ORR over PtNi alloy nanowires, a combination

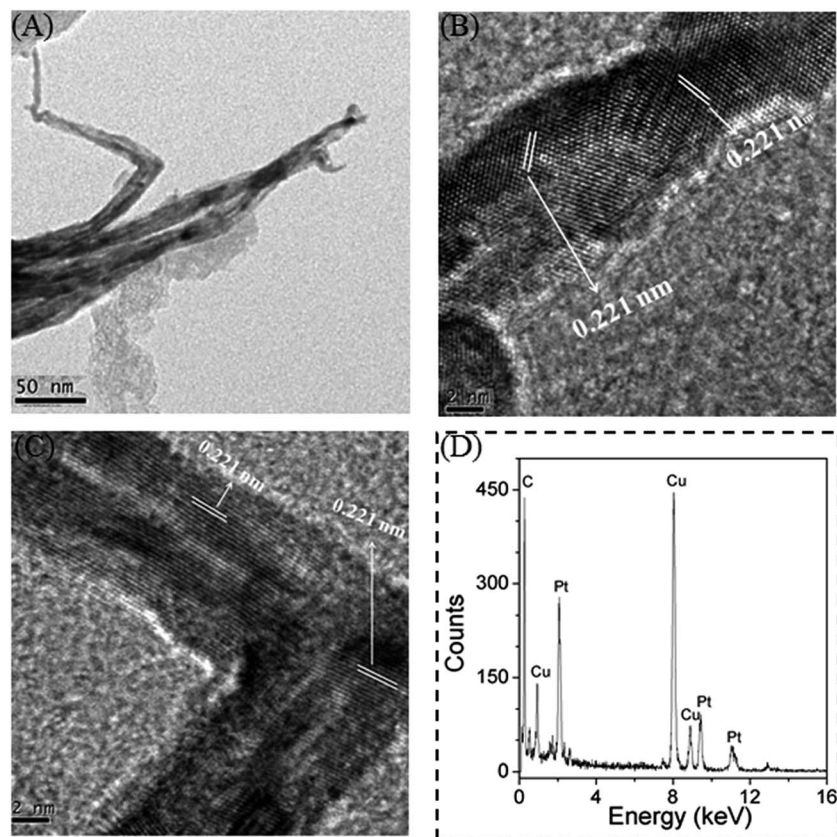


Fig. 8 (A) TEM images after 5000 cycles ( $4.2 \pm 0.5$  nm); (B and C) HR-TEM image, the lattice fringes of (111): 0.221 nm. (D) TEM-EDX of the Pt<sub>59</sub>Ni<sub>41</sub>/C after 5000 cycles. Pt/Ni = 90.1/9.9 (confirmed by ICP-OES and TEM-EDX). The standard deviation: 0.1–0.5%.

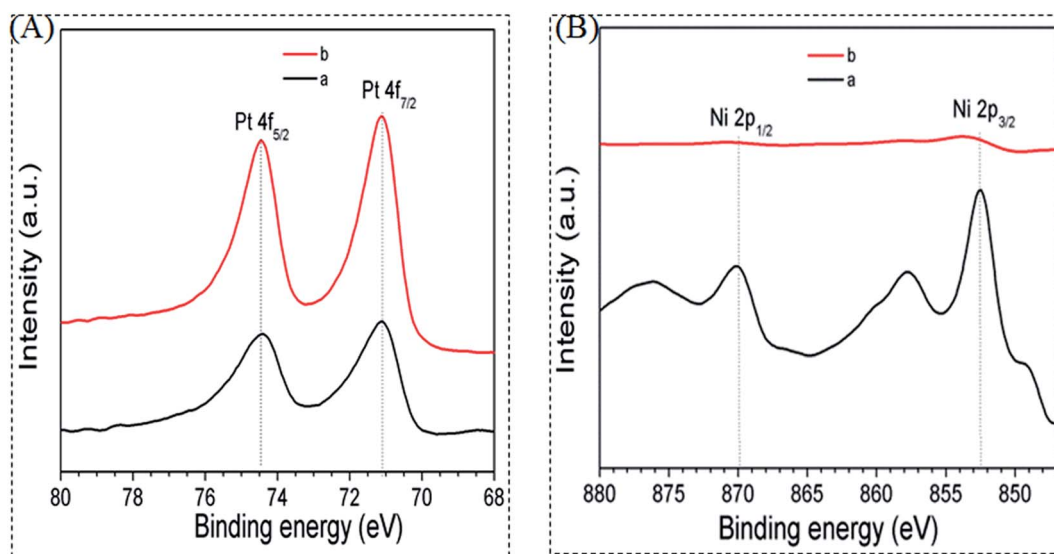


Fig. 9 XPS spectra in the regions of (A) Pt 4f and (B) Ni 2p (a: before; b: after 5000 cycles). The international standard (C 1s) was used to calibrate the peak position.

of bifunctional synergy and atomic-scale alloying<sup>39</sup> was considered in terms of the strain and ligand effects. The width of the surface d-band can be changed by the strain and the ligand effect, which subsequently leads to up or down shift in

energy in order to keep the band filling unchanged. The introduction of Ni lowers the energy of the d-band for Pt and creates d-band vacancies, which would lower the binding energy for oxygen-containing species, which in turn facilitates the

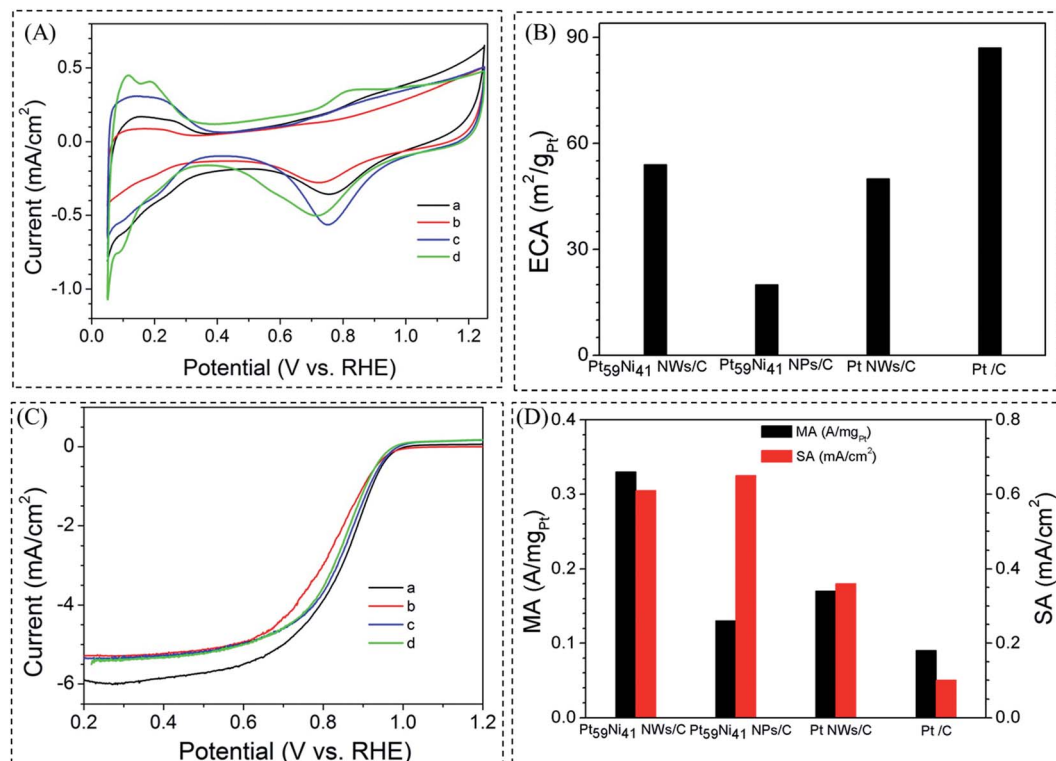
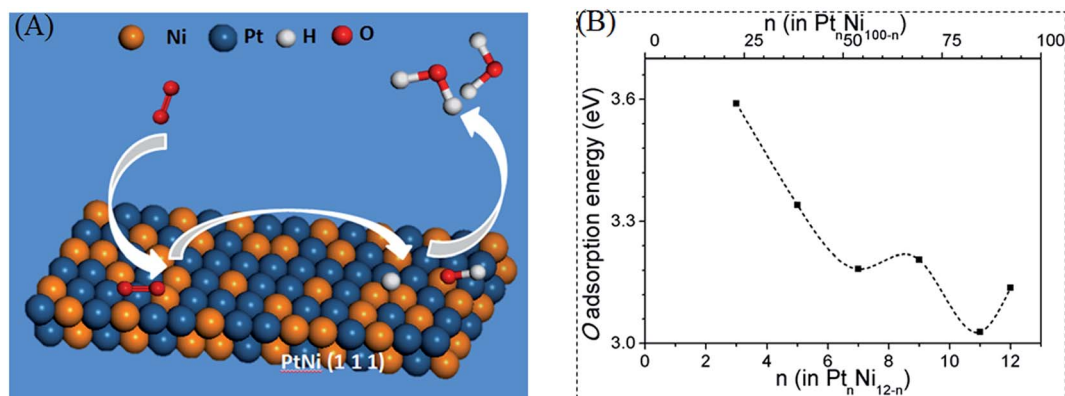


Fig. 10 (A) CV and (C) RDE curves of Pt<sub>59</sub>Ni<sub>41</sub> NWs/C (a, black), Pt<sub>59</sub>Ni<sub>41</sub>NPs/C (b, red), Pt NWs/C (c, blue) and commercial Pt/C (d, green) (electrode: glassy carbon (0.196 cm<sup>2</sup>) inked with 10 μg catalysts; electrolyte: 0.1 M HClO<sub>4</sub> saturated with N<sub>2</sub> for CV and 0.1 M HClO<sub>4</sub> saturated with O<sub>2</sub> for RDE; scan rate: 50 mVs<sup>-1</sup> (CV), and 10 mVs<sup>-1</sup> (RDE); rotation speed: and 1600 rpm); (B) ECA values vs. Pt%. (D) Mass activity and specific activity data at 0.900 V (vs. the RHE).



Scheme 1 (A) A schematic illustration of the catalytic synergy for the oxygen reduction reaction over PtNi NWs featuring the (111) facet; (B) adsorption energy of molecularly adsorbed O on Pt<sub>n</sub>Ni<sub>12-n</sub> clusters ( $n = 1-12$ ) obtained by DFT.

completion of the ORR.<sup>48</sup> For the ORR over the PtNi alloy NW catalysts featuring predominantly (111) facets (Scheme 1A), the relatively weak binding of the adsorbed oxygen species facilitates their diffusion to adjacent sites on the (111) facet. The removal of the adsorbed intermediate species (*e.g.*, O and OH) formed after the cleavage of the O–O bond is favored by a weaker adsorption energy of the Pt–O species.<sup>49</sup> The adsorption energy of the intermediate O species in the ORR ( $E_{\text{O}}$ ) on the catalyst surfaces with different catalyst compositions (Scheme

1B) indicates that the adsorption of O on Pt<sub>3</sub>Ni<sub>9</sub> is stronger than those on Pt<sub>5</sub>Ni<sub>7</sub>, Pt<sub>7</sub>Ni<sub>5</sub>, Pt<sub>9</sub>Ni<sub>3</sub>, Pt<sub>11</sub>Ni<sub>1</sub> and Pt<sub>12</sub>. In general, a moderate M–O interaction is responsible for the catalyst's high activity. Pt<sub>7</sub>Ni<sub>5</sub> shows intermediate value for the adsorption of O on the Pt<sub>n</sub>Ni<sub>12-n</sub> model. Pt<sub>7</sub>Ni<sub>5</sub> has a higher catalytic activity. By incorporating Ni in Pt, there is a compressive strain as a result of the smaller atomic size of Ni,<sup>50</sup> and the charge transfer between Pt and Ni would lower the d-band center for Pt,<sup>34</sup> weakening the O binding.

## 4. Conclusion

In summary, PtNi nanowires of different bimetallic compositions were synthesized without the use of any surfactant and were shown to exhibit enhanced electrocatalytic activity without any post-synthesis treatment. The synthetic route is simple, reproducible, and scalable for the preparation of PtNi NWs. Ultrathin PtNi NWs featuring composition-tunable and (111) (200)-dominant facets have been demonstrated for the first time as composition- and facet-tunable catalysts for the ORR. The ORR activity is shown to exhibit a maximum activity at a Pt : Ni ratio of  $\sim 3 : 2$ . In comparison with the catalysts derived from the nanoparticle counterpart with a similar composition, the nanowire catalysts were shown to display a higher catalytic activity and stability for the ORR as a result of the composition-dependent atomic-scale alloying and faceting properties. These findings are significant considering the potential scale-up hydrothermal synthesis of metal and alloy nanowires<sup>14,51</sup> for applications in catalysis.

## Acknowledgements

This work was supported by the Department of Energy (DOE)–Basic Energy Science Grant (DE-SC0006877), the National Science Foundation (CHE 1566283), and the National Natural Science Foundation of China (51271074). Synchrotron X-ray diffraction was performed at Beamline 11-ID-C of the Advanced Photon Source, a U.S. DOE Office of Science User Facility, which is operated for the DOE Office of Science by Argonne National Laboratory under Contract No. DE-AC02-06CH11357.

## References

- 1 K. Sasaki, H. Naohara, Y. Cai, Y. M. Choi, P. Liu, M. B. Vukmirovic, J. X. Wang and R. R. Adzic, *Angew. Chem., Int. Ed.*, 2010, **49**, 8602–8607.
- 2 H. Li, Y. Y. Luk and M. Mrksich, *Langmuir*, 1999, **15**, 4957–4959.
- 3 A. Morozan, B. Josselme and S. Palacin, *Energy Environ. Sci.*, 2011, **4**, 1238–1254.
- 4 I. Rawal and A. Kaur, *Sens. Actuators, A*, 2013, **203**, 92–102.
- 5 D. Zhen, B. Zhao, H. C. Shin, Y. Bu, Y. Ding, G. He and M. Liu, *Adv. Mater. Interfaces*, 2017, 1700146.
- 6 B. Zhao, L. Zhang, D. Zhen, S. Yoo, Y. Ding, D. Chen, Y. Chen, Q. Zhang, B. Doyle, X. Xiong and M. Liu, *Nat. Commun.*, 2017, **8**, 14586.
- 7 M. F. Li, Z. P. Zhao, T. Cheng, A. Fortunelli, C. Y. Chen, R. Yu, Q. H. Zhang, L. Gu, B. V. Merinov, Z. Y. Lin, E. B. Zhu, T. Yu, Q. Y. Jia, J. H. Guo, L. Zhang, W. A. Goddard III, Y. Huang and X. F. Duan, *Science*, 2016, **354**, 1414–1419.
- 8 C. Koenigsmann, A. C. Santulli, K. P. Gong, M. B. Vukmirovic, W. P. Zhou, E. Sutter, S. S. Wong and R. R. Adzic, *J. Am. Chem. Soc.*, 2011, **133**, 9783–9795.
- 9 S. J. Guo, S. Zhang, X. L. Sun and S. H. Sun, *J. Am. Chem. Soc.*, 2011, **133**, 15354–15357.
- 10 B. Li, Z. Y. Yan, D. C. Higgins, D. J. Yang, Z. W. Chen and J. X. Ma, *J. Power Sources*, 2014, **262**, 488–493.
- 11 S. H. Sun, G. X. Zhang, D. S. Geng, Y. G. Chen, R. Y. Li, M. X. Cai and L. Sun, *Angew. Chem., Int. Ed.*, 2011, **50**, 422–426.
- 12 L. Dubau, T. Asset, R. hattot, C. Bonnaud, V. Vanpeene, J. Nelayah and F. Maillard, *ACS Catal.*, 2015, **5**, 5333–5341.
- 13 C. H. Cui, L. Gan, H. H. Li, S. H. Yu, M. Heggen and P. Strasser, *Nano Lett.*, 2012, **12**, 5885–5889.
- 14 F. F. Chang, S. Y. Shan, V. Petkov, Z. Skeete, A. L. Lu, J. Ravid, J. F. Wu, J. Luo, G. Yu, Y. Ren and C. J. Zhong, *J. Am. Chem. Soc.*, 2016, **138**, 12166–12175.
- 15 B. Y. Xia, H. B. Wu, Y. X. Yan, W. Lou and X. Wang, *J. Am. Chem. Soc.*, 2013, **135**, 9480–9485.
- 16 J. P. Lai, L. Zhang, W. J. Qi, J. M. Zhao, M. Xu, W. Y. Gao and G. B. Xu, *ChemCatChem*, 2014, **6**, 2253–2257.
- 17 S. Y. Shan, V. Petkov, L. F. Yang, J. Luo, P. Joseph, D. Mayzel, B. Prasai, L. Y. Wang, M. Engelhard and C. J. Zhong, *J. Am. Chem. Soc.*, 2014, **136**, 7140–7151.
- 18 B. Fang, B. N. Wanjala, X. Hu, J. Last, R. Loukrakpam, J. Yin, J. Luo and C. J. Zhong, *J. Power Sources*, 2011, **196**, 659–665.
- 19 M. R. Xia, W. Ding, K. Xiong, L. Li, X. Q. Qi, S. G. Chen, B. S. Hu and Z. D. Wei, *J. Phys. Chem. C*, 2013, **117**, 10581–10588.
- 20 L. Wang, Y. Wang, S. Q. Song and P. K. Shen, *Chin. J. Catal.*, 2009, **30**, 433–439.
- 21 L. C. Wang, J. I. Williams, T. Lin and C. J. Zhong, *Catalysis Today*, 2011, **165**, 150–159.
- 22 L. Dubau, J. Nelayah, S. Moldovan, O. Ersen, P. Bordet, J. Drnec, T. Asset, R. Chattot and F. Maillard, *ACS Catal.*, 2016, **6**, 4673–4684.
- 23 F. Calle-Vallejo, J. Tymoczko, V. Colic, Q. H. Vu, M. D. Pohl, K. Morgenstern, D. Loffreda, P. Sautet, W. Schuhmann and A. S. Bandarenka, *Science*, 2015, **350**, 185–189.
- 24 E. A. Lord and S. Ranganathan, *J. Non-Cryst. Solids*, 2004, **334–335**, 121–125.
- 25 Y. H. Zhu, J. T. He, C. Shang, X. H. Miao, J. F. Huang, Z. P. Liu, H. Chen and Y. Y. Han, *J. Am. Chem. Soc.*, 2014, **136**, 12746–12752.
- 26 J. J. Velázquez-Salazar, R. Esparza, S. J. Mejía-Rosales, R. Estrada-Salas, A. Ponce, F. L. Deepak, C. Castro-Guerrero and M. José-Yacamán, *ACS Nano*, 2011, **8**, 6272–6278.
- 27 R. Mendoza-Cruz, L. Bazán-Díaz, J. J. Velázquez-Salazar, G. Plascencia-Villa, D. Bahena-Urbe, J. Reyes-Gasga, D. Romeu, G. Guisbiers, R. Herrera-Becerra and M. José-Yacamán, *Nano Lett.*, 2016, **16**, 1568–1573.
- 28 J. Luo, J. Yin, R. Loukrakpam, B. N. Wanjala, B. Fang, S. Shan, L. Yang, M. Nie, M. Ng, J. Kinzler, Y. S. Kim, K. K. Luo and C. J. Zhong, *J. Electroanal. Chem.*, 2013, **688**, 196–206.
- 29 B. Wanjala, J. Luo, R. Loukrakpam, P. N. Njoki, D. Mott, C. J. Zhong, M. Shao, L. Protsailo and T. Kawamura, *J. Phys. Chem. C*, 2010, **114**, 17580–17590.
- 30 B. Fang, B. N. Wanjala, J. Yin, R. Loukrakpam, J. Luo, X. Hu, J. Last and C. J. Zhong, *Int. J. Hydrogen Energy*, 2012, **37**, 4627–4632.

- 31 B. Fang, J. Luo, P. N. Njoki, R. Loukrakpam, B. N. Wanjala, J. Hong, J. Yin, X. Hu, J. Last and C. J. Zhong, *Electrochim. Acta*, 2010, **55**, 8230–8236.
- 32 T. W. Chen, J. X. Kang, D. F. Zhang and L. Guo, *RSC Adv.*, 2016, **6**, 71501–71506.
- 33 R. Devivaraprasad, R. Ramesh, N. Naresh, T. Kar, R. K. Singh and M. Neergat, *Langmuir*, 2014, **30**, 8995–9006.
- 34 D. F. Vliet, C. Wang, D. Tripkovic, D. Strmcnik, X. F. Zhang, M. K. Debe, R. T. Atanasoski, N. M. Markovic and V. R. Stamenkovic, *Nat. Mater.*, 2012, **11**, 1051–1058.
- 35 V. R. Stamenkovic, B. Fowler, S. Mun, G. F. Wang, P. N. Ross, C. A. Lucas and N. M. Markovic, *Science*, 2007, **315**, 493–497.
- 36 J. F. Wu, S. Y. Shan, V. Petkov, B. Prasai, H. Cronk, P. Joseph, J. Luo and C. J. Zhong, *ACS Catal.*, 2015, **5**, 5317–5327.
- 37 J. F. Wu, S. Y. Shan, J. Luo, P. Joseph, V. Petkov and C. J. Zhong, *ACS Appl. Mater. Interfaces*, 2015, **7**, 25906–25913.
- 38 J. Zhang, H. Yang, J. Fang and S. Zou, *Nano Lett.*, 2010, **10**, 638–644.
- 39 C. Cui, L. Gan, M. Heggen, S. Rudi and P. Strasser, *Nat. Mater.*, 2013, **12**, 765–771.
- 40 C. Wang, M. Chi, G. Wang, D. van der Vliet, D. Li, K. More, H. H. Wang, J. A. Schlueter, N. M. Markovic and V. R. Stamenkovic, *Adv. Funct. Mater.*, 2011, **21**, 147–152.
- 41 J. Kim, S. W. Lee, C. Carlton and Y. Shao-Horn, *Electrochem. Solid-State Lett.*, 2011, **14**, 110–113.
- 42 R. Loukrakpam, J. Luo, T. He, Y. S. Chen, Z. C. Xu, P. N. Njoki, B. N. Wanjala, B. Fang, D. Mott, J. Yin, J. Klar, B. Powell and C. J. Zhong, *J. Phys. Chem. C*, 2011, **115**, 1682–1694.
- 43 Z. W. Chen, D. Higgins, A. P. Yu, L. Zhang and J. J. Zhang, *Energy Environ. Sci.*, 2011, **4**, 3167–3192.
- 44 W. K. Suha, P. Ganesana, B. Sonb, H. Kima and S. Shanmugam, *Int. J. Hydrogen Energy*, 2016, **41**, 12983–12994.
- 45 W. Z. Li and P. Haldar, *Electrochem. Solid-State Lett.*, 2010, **13**, 47–49.
- 46 F. Hasche, M. Oezaslan and P. Strasser, *J. Electrochem. Soc.*, 2012, **159**, 25–34.
- 47 S. J. Bae, S. J. Yoo, Y. Lim, S. Kim, Y. Lim, J. Choi, K. S. Nahm, S. J. Hwang, T. H. Lim, S. K. Kim and P. Kim, *J. Mater. Chem.*, 2012, **22**, 8820–8825.
- 48 J. R. Kitchin, J. K. Nørskov, M. A. Barteau and J. G. Chen, *Phys. Rev. Lett.*, 2004, **93**, 156801.
- 49 M. H. Shao, P. Liu, J. L. Zhang and R. R. Adzic, *J. Phys. Chem. B*, 2007, **111**, 6772–6775.
- 50 X. Zhang and G. Lu, *J. Phys. Chem. Lett.*, 2014, **5**, 292–297.
- 51 Z. C. Li, A. J. Gu, M. Y. Guan, Q. F. Zhou and T. M. Shang, *Colloid Polym. Sci.*, 2010, **288**, 1185–1191.